



# Self-assembled (Ni/Cu, Ti)-YSZ with potential applications for IT-SOFCs: Catalytic and electrochemical assessment



Simona Somacescu<sup>a,\*</sup>, Laura Navarrete<sup>b</sup>, Mihaela Florea<sup>c</sup>, Jose Maria Calderon-Moreno<sup>a</sup>, Jose Manuel Serra<sup>b,\*\*</sup>

<sup>a</sup> "Ilie Murgulescu" Institute of Physical Chemistry, Romanian Academy, Surface Chemistry and Catalysis Laboratory, Spl. Independentei 202, 060021, Bucharest, Romania

<sup>b</sup> Instituto de Tecnología Química (Universidad Politécnica de Valencia – Consejo Superior de Investigaciones Científicas), Avenida de los Naranjos s/n, 46022, Valencia, Spain

<sup>c</sup> University of Bucharest, Faculty of Chemistry, Department of Organic Chemistry, Biochemistry and Catalysis, B-dul Regina Elisabeta 4-12, Bucharest, Romania

## ARTICLE INFO

### Article history:

Received 12 July 2016

Received in revised form

18 August 2016

Accepted 20 August 2016

Available online 22 August 2016

### Keywords:

Surfactant

Partial oxidation of methane

Ionic conductivity

Electrochemical properties

## ABSTRACT

(Ni/Cu, Ti)-YSZ samples were synthesized by self-assembling synthesis route using Triton X as template and thermal treated at 700 °C and 900 °C in air flow. Microstructure, surface chemistry and electrochemical properties were assessed by XRD, N<sub>2</sub> adsorption-desorption, SEM, TEM, XPS, TPR-H<sub>2</sub> and DC conductivity measurements. The synthesis route leads to a very well incorporation of Ti into YSZ lattice. X-ray diffraction shows that (Cu, Ti)-YSZ exhibits a phase transition, from cubic fluorite phase to monoclinic, when the calcination temperature rises from 700 °C to 900 °C, while (Ni, Ti)-YSZ exhibits only two cubic phases, with a main fluorite-type phase and a secondary isostructural phase with bunsenite (NiO) for both calcination temperatures. The partial oxidation of methane was performed in the temperature range 250–900 °C, and the results can be summarized as follows: i) for the (Cu, Ti)-YSZ samples it was found that the phase transformation from cubic fluorite to monoclinic favors an increase in methane conversion as well as the selectivity to CO; ii) the samples containing Ni are more active than those containing Cu, with 90% methane conversion at 750 °C as compared to 75% conversion, respectively. Regarding the total conductivity of the material synthesized, two different behaviors were obtained depending on the composition; the (Ni, Ti)-YSZ maintained a prevailing ionic conductivity, whereas the (Cu, Ti)-YSZ exhibited mainly n-type conductivity. The ionic conductivity of Ni-based sample is beneficial for the partial oxidation of methane due to the oxygen vacancies generated on the surface of the material, which plays a fundamental role in the O<sub>2</sub> activation mechanism and is in accordance with higher catalytic activity observed for the Ni containing sample.

© 2016 Elsevier B.V. All rights reserved.

## 1. Introduction

Solid oxide fuel cells (SOFC) offer a promising way of converting chemical energy into electrical energy with high efficiency [1,2]. SOFCs consist of three main parts: an anode, a cathode and an electrolyte. The electrolyte possesses high ionic or protonic conductivity, whereas electrodes should have both high ionic/protonic and electronic conductivity. Furthermore, both electrodes have to be

catalytically active for the oxidation and reduction in anode and cathode, respectively, and to possess enough porosity to facilitate the gas diffusion. They operate at elevated temperatures (550–1000 °C) to ensure adequate conductivity and catalytic activity of all the components of the device. In the fuel cell operation, air or oxygen is fed as oxidant whereas hydrogen is usually used as fuel.

Although this is clearly a green technology, there is a huge challenge related to competitiveness with existing technologies, especially with respect to the cost per kWh supplied. Also, the anode needs to operate at high temperatures and under strong reducing atmosphere, that imposes restrictions on the anode type material selection and requires special challenges related to its chemical stability and materials degradation [3]. Over the last

\* Corresponding author.

\*\* Corresponding author.

E-mail addresses: [ssimona@icf.ro](mailto:ssimona@icf.ro), [somacescu.simona@gmail.com](mailto:somacescu.simona@gmail.com) (S. Somacescu), [jmserra@itq.upv.es](mailto:jmserra@itq.upv.es) (J.M. Serra).

decades, a lot of work has been invested in the development of alternative anode materials with high redox stability and longer lifetime, but some problems still exist due to their low catalytic activity and electronic conductivity. As a consequence, to find an ideal candidate for anode and low-cost manufacturing routes represents challenging tasks for scientific community. It is well known that the synthesis routes for the catalyst production influence hugely the overall catalyst activity and the selectivity towards different reaction products [4]. The material properties which can affect the sintering characteristics and anode microstructure, like particle size, surface area, distribution of metal on the support, conductivity, etc., are influenced by the synthesis adopted methods [5]. In this regard, Jung et al. [6] showed that indeed the anode performance depends on the synthesis route. On the other hand, it is well known that the surfactants are used to obtain the desired porous structure and to decrease the particles size [7–9]. The formation of ordered ceramic nanostructures with tunable morphology and composition for SOFC anode can provide high cell performance. Different configurations are already employed for the anode manufacture; the most common is a cermet electrode made of a ceramic and a metal phase. In many cases, metals, as Ni or Cu, for example, which represent the current collector, are deposited by impregnation [10]. However, this method presents some disadvantages as low dispersion and increased sintering tendency, with clusters formation as a consequence. In order to improve the electrochemical performance for the cermets based on Ni and Cu, different other synthesis routes were approached [11–13]. Thus, Ni:Cu:YSZ = 40:20:40 fabricated by high-energy ball-milling of Ni, Cu, and YSZ powder [12] showed an improvement of the electrical conductivity as results of the well-connected Ni/Cu/YSZ particles achieved through an increased ball-milling time. Also, it has been highlighted the effect of the composition on the electrical conductivity for Cu/YSZ composite [13] synthesized by the same method. A recent report revealed an excellent SOFC performance for Ni<sub>0.5</sub>Cu<sub>0.5</sub>O<sub>x</sub> coated tubular YSZ prepared by hard template method combined with wet impregnation method [11].

In this study (Ni/Cu, Ti)-YSZ anodes were synthesized by a facile and low-cost synthesis route. This route involves a self-assembling of the elements using Triton X100 as template. The self-assembled method helps to avoid the sintering phenomenon by providing a high Ni or Cu dispersion into an oxidic matrix, providing many oxygen vacancies. The electronic conductivity can be expected by the presence of Cu<sup>0</sup> species resulted from strong reducing environments, but also by reduction of Ti<sup>4+</sup> to Ti<sup>3+</sup> rising the quantity of free electrons. Finally, the incorporation of species with lower valence as Y<sup>3+</sup> can provide the ionic conductivity. The structural properties and surface chemistry of these new materials, as well as the electrochemical and catalytic performance, were assessed. The surfactant was used to obtain the desired porous structure and to decrease the particle size in order to improve the SOFCs performance.

## 2. Material and methods

### 2.1. Materials synthesis

(Ni/Cu, Ti)-YSZ (20 mol. % Ni/Cu, 10 mol.% Ti) materials were

synthesized by a self-assembling method, using a nonionic surfactant – Triton X100 as template. In this synthesis route Zirconium propoxide, yttrium acetylacetonate, titanium (IV) isopropoxide, nickel acetyl acetonate and copper acetate were used as inorganic precursors. 1-Propanol was used as solvent. The nonionic surfactant was dispersed in alcohol under strong stirring. The inorganic precursors were dissolved in 1-Propanol and added maintaining stirring conditions at room temperature. The gels formed were dried several days at 50 °C, followed by an increase of temperature at 100 °C. All samples were calcined in air at 700 °C and 900 °C, respectively. The (Ni/Cu, Ti)-YSZ samples are labeled as below (see Table 1).

### 2.2. Characterization methods

**X-Ray diffraction (XRD) analyses** were carried out on a Schimadzu XRD-7000 diffractometer using Ni-filtered Cu K $\alpha$  radiation with  $\lambda = 1.5418$  Å. The tube source was operated at 40 kV and 30 mA. Scans were taken in the 2 $\theta$  range of 10–80° with a step size of 0.02° and scan time of 2°/min. Crystalline phase were identified by the comparison of the XRD patterns with the JCPDS database. The crystallite sizes were calculated using Scherrer's formula  $D = k\lambda/\beta \cos \theta$ , where  $D$  is the average crystallite size,  $k$  a constant equal to 0.89,  $\lambda$  the wavelength of X rays and  $\beta$  is the corrected half width.

**Porosity Analysis (BET)** - Brunauer–Emmett–Teller adsorption–desorption isotherms of N<sub>2</sub> were obtained at –196 °C over a wide relative pressure range from 0.01 to 0.995 with a volumetric adsorption analyzer ASAP-2020 manufactured by Micromeritics. The sample was degassed further under vacuum at 150 °C overnight prior to nitrogen adsorption. Desorption isotherm was used to estimate the pore-size distribution.

**Scanning electron microscopy (SEM)**. The images were recorded with a Field Emission Gun FEI Quanta 3D microscope operating at 2 kV.

**Transmission electron microscopy (TEM)**. TEM micrographs were recorded with a HITACHI HT800 apparatus equipped with a Link energy dispersive X-ray (EDX) system and operated at an accelerating voltage of 200 kV. The powders were ultrasonicated in ethanol and a drop of the solution dried on a carbon coated microgrid before measurements.

**The reduction behavior** was studied by H<sub>2</sub>-TPR in a Micromeritics Autochem 2910 equipment. About 50 mg of sample (particle size 0.25–0.42 mm) was initially flushed with Ar at room temperature for 30 min. Then, the gas was switched to the reductive mixture of 10 vol% H<sub>2</sub> in Ar (50 mL min<sup>–1</sup>) and the temperature linearly increased from RT to 900 °C at a heating rate of 10 °C min<sup>–1</sup>. Water formed in the reduction was retained in a 2-propanol/N<sub>2</sub>(l) trap and the H<sub>2</sub> consumption rate was monitored in a thermal conductivity detector (TCD) previously calibrated using the reduction of CuO as reference.

**X-ray photoelectron spectroscopy (XPS)** - Surface analysis performed by X-ray photoelectron spectroscopy (XPS) was carried out on PHI Quantera equipment with a base pressure in the analysis chamber of 10<sup>–9</sup> Torr. The X-ray source was monochromatized Al K $\alpha$  radiation (1486.6 eV) and the overall energy resolution is estimated at 0.70 eV by the full width at half-maximum (FWHM) of the

**Table 1**  
Compositions of the sample studied and abbreviation name.

Name	Ni content (mol. %)	Cu content (mol. %)	Ti content (mol. %)	T calcination (°C)
CTST700	–	20	10	700
CTST900	–	20	10	900
NTST700	20	–	10	700
NTST900	20	–	10	900

Au4f7/2 photoelectron line (84eV). Although the charging effect was minimized by using a dual beam (electrons and Ar ions) as neutralizer, the spectra were calibrated using the C1s line (BE = 284.8 eV) of the adsorbed hydrocarbon on the sample surface (C–C or (CH)<sub>n</sub> bondings). As this spectrum was recorded at the start and the end of each experiment the energy calibration during experiments was quite reliable.

### 2.3. Catalytic activity measurements

The catalytic activity for partial oxidation of methane (POM) was evaluated in a continuous fixed-bed tubular reactor (length of 300 mm and i.d. of 9 mm, Hasteloy X tube), equipped with a thermo well in the center of the catalyst bed. The experiments were typically carried out in a downflow system at atmospheric pressure. The catalyst powder was placed between a two layers of quartz wool and was first activated for 2 h in air, at 800 °C before the reaction, and then the reactor was cooled down to 200 °C. Reactions were conducted at different temperatures starting from 200 °C, using a feed consisting of 13.33% CH<sub>4</sub>; 6.66% O<sub>2</sub>; 80% N<sub>2</sub> at a total flow of 37.5 mL min<sup>-1</sup> and GHSV of 22500 h<sup>-1</sup>. The products were analyzed online by a gas chromatograph (Shimadzu GC-2014) equipped with a TCD and FID detectors and two capillary columns Molecular Sieve 5A and Poraplot Q (length, 60 m; internal diameter, 0.32 mm; film thickness, 0.5 μm). Activity and selectivity results were calculated according to the equations given below:

$$\text{CH}_4 \text{ conversion (\%)} = \frac{\mu_{\text{CH}_4\text{in}} - \mu_{\text{CH}_4\text{out}}}{\mu_{\text{CH}_4\text{in}}} \times 100 \quad (1)$$

$$\text{CO selectivity (\%)} = \frac{\mu_{\text{CO}}}{\mu_{\text{CH}_4\text{in}} - \mu_{\text{CH}_4\text{out}}} \times 100 \quad (2)$$

### 2.4. Electrochemical characterization

#### 2.4.1. Conductivity measurements

Rectangular probes of the powders, CTST and NTST, were uniaxially pressed and subsequently sintered for 10 h at 1000 °C and 1300 °C respectively in air. Electrical conductivity measurements were conducted by standard fourpoint DC technique. Silver paste and wires were used to obtain the electronic contact. A constant current was supplied by Keithley 2601 and the voltage was detected by a multimeter (Keithley 3706).

#### 2.4.2. Electrochemical impedance spectroscopy (EIS) measurements

Screen-printing ink made of CTST anode was prepared by mixing in a three roll mill, the CTST powder and an ethylcellulose (6%

wt.) solution in terpineol in a weight ratio of 1:2. The ink was screenprinted on both sides of 8YSZ 0.15 mm-thick fully-dense electrolytes provided by Kerafol (Germany). Porous electrodes were obtained after calcining the resulting screen-printed layers at 950 °C for 2 h. A top screen-printed gold mesh was applied on the electrodes in order to ensure proper current collection.

As-fabricated symmetrical cells were tested by means of electrochemical impedance spectroscopy measurements using a 0 V DC – 20 mV AC amplitude signal using a Solartron 1470E/1455 FRA device. Electrochemical measurements were performed in air in the 600–900 °C temperature range. Electrode microstructure was analyzed by SEM imaging in a ULTRA 55 ZEISS microscope FESEM.

## 3. Results and discussion

### 3.1. Physico-chemical characterization

The indexed XRD pattern of CTST700, shown in Fig. 1a, indicates the formation of a bi-phasic nanocrystalline powder of stabilized cubic zirconia and tenorite. The main phase corresponds to a zirconia-based cubic phase of fluorite type (Fm3m), with lattice parameter  $c = 5.073 \text{ \AA}$ . XRD detects also the presence of a secondary phase (~20 mol.%, marked \* in the indexed pattern in Fig. 1) with monoclinic symmetry (C2/c), isostructural with tenorite (CuO), with slightly enlarged lattice parameters,  $a = 4.695 \text{ \AA}$ ,  $b = 3.433 \text{ \AA}$ ,  $c = 5.141 \text{ \AA}$ ,  $\alpha = \beta = 90^\circ$ ,  $\gamma = 99.470^\circ$ . Both phases have small nanocrystallite size, around 8 nm for the zirconia-based fluorite-type phase and 12 nm for the copper oxide-based tenorite-type phase, respectively. In spite of the incorporation of titania into the YSZ lattice, the high temperature cubic structure remains stabilized at room temperature due to the small size of the nanocrystallites.

The XRD pattern of CTST after thermal treatment at 900 °C, CTST900, can be indexed to a monoclinic zirconia-based phase and tenorite as secondary phase (~20 mol.%) (Fig. 1a). Thermal treatment at 900 °C results with the significant growth of crystalline sizes for both the zirconia-based and CuO phases (30 nm and 25 nm respectively), thus leading to the spontaneous phase transformation of the cubic zirconia phase into monoclinic, caused most likely by crystallite growth. The absence of traces of any titanium containing phase and the spontaneous formation of the monoclinic structure indicates that TiO<sub>2</sub> have incorporated in YSZ forming a solid solution phase, previous studies have demonstrated that the solid solubility limit of TiO<sub>2</sub> in YSZ nanoparticles is indeed much higher than the concentration of TiO<sub>2</sub> in the zirconia-based phase in CTST [14]. There is no change in the lattice parameters of the CuO phase, indicating that composition of the tenorite phase remains unchanged.

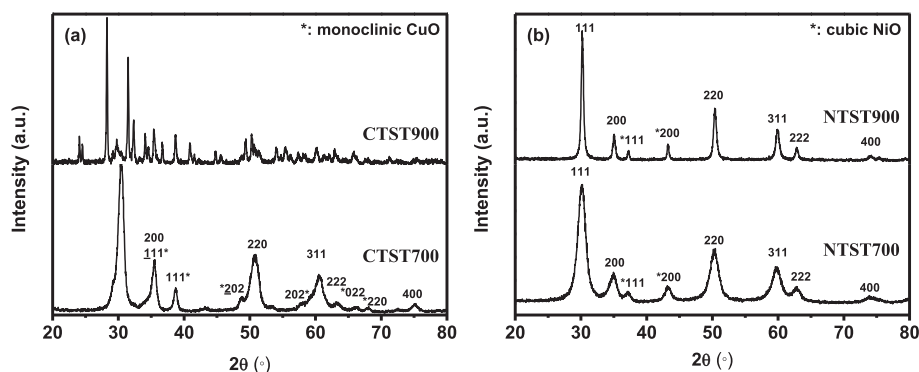


Fig. 1. XRD patterns for CTST (a) and NTST (b) samples calcined at 700 and 900 °C.

The XRD pattern of sample NTST700 (Fig. 1b) corresponds to two cubic phases, a main fluorite-type phase (Fm3m), and a secondary phase (~15 mol%, also Fm3m, marked with \* in Fig. 1b) isostructural with bunsenite (NiO). The fluorite has a lattice parameter  $c = 5.131 \text{ \AA}$  whereas the lattice parameter of the bunsenite is  $c = 4.184 \text{ \AA}$ , bigger than  $c = 4.177 \text{ \AA}$  for standard bunsenite (JCPDS Card 04-0835). In addition, both phases have similar nanoscale crystallite size, around 5 nm. The XRD pattern of NTST after annealing the sample at 900 °C (NTST900, Fig. 1b) can be indexed to the same two phases, fluorite and bunsenite, without changes in the lattice parameters. As a result of the thermal treatment at 900 °C a clear peak width reduction is observed, evidencing the significant crystal growth of both phases, from 5 nm to around 15 nm. Ni incorporated into YSZ cubic matrix was found as strongly dependent on the synthesis route and Ni relative concentration, as well. Indeed, in our recent work on mesoporous Ni doped (CeO<sub>2-δ</sub>)-YSZ (5 mol% Ni oxide, 10 mol% ceria) obtained by hydrothermal treatment [15] we highlighted that Ni was incorporated into the cubic structure without any trace of NiO as secondary phase as obtained by self-assembled method presented in this study.

In Table 2 are gathered the structural and textural properties of the studied samples.

As seen in Table 2, for the samples calcined at 700 °C, surface areas of 15 and 66 m<sup>2</sup>/g were observed for the CTST and NTST, respectively. It seems that NiO acts as an inhibitor for the coarsening of YSZ during the calcination [16] and therefore higher surface area is observed for the containing Ni sample. As expected, after calcinations at higher temperatures, the surface area decreased, mainly due to the thermal sintering processes. Nevertheless, the NTST900 presents higher surface area than CTST900, in good agreement with smaller crystallite size measured from XRD data and reported in Table 2.

Brunauer–Emmett–Teller (BET) analysis of the NTST700 and CTST700 samples isotherms confirms the presence of the mesoporous structure (Fig. 2a, b). The shape of the N<sub>2</sub> adsorption-desorption isotherms, is characterized by a hysteresis loop at higher partial pressures. This kind of isotherm (type IV according to IUPAC) is specific to mesoporous solids. The initial part of the isotherm is attributed to monolayer-multilayer adsorption and the hysteresis loop is associated with capillary condensation taking place in mesopores. The pore sizes distributions derived from the desorption isotherm show a narrow pore size distribution for NTST700 sample, while for the CTST700 the distribution is wider (Fig. 2c, d). The thermal treatment has a major influence on the porous structure, giving rise to macroporous materials, as indicated by type III isotherm (Fig. 2a, b).

SEM micrographs of the CTST700 and NTST700 powders as processed are shown in Fig. 3a, b. Large clusters with crystalline framework of ultra fine particles and porous structure can be observed in the micrographs. The samples show excellent homogeneity of the pores and nanocrystallite sizes in all analyzed regions.

Fig. 3c, d show TEM micrographs of NTST700. The low resolution TEM micrograph (Fig. 3c) shows the nanocrystalline powder with

typical sizes around 5 nm, which correspond to the size of single nanocrystallites determined from XRD measurements. Porosity arises from spaces left between nanocrystallites, seen as clearer areas in TEM micrographs. The intercrystalline porosity measured from N<sub>2</sub> adsorption/desorption have somewhat bigger sizes than single nanocrystallite size, the high resolution TEM measurements (Fig. 3d) confirm the presence and size of intercrystalline porosity in the mesoporous powder.

The reduction behavior was investigated with H<sub>2</sub>-TPR. The TPR profile for each sample is presented in Fig. 4 a–d.

The thermal treatment at 700 °C for samples containing Cu, leads to Cu species reducible at low temperature, ~200 °C, and until 300 °C the Cu is completely reduced (Fig. 4a). This reduction peak can be associated with the reduction of CuO in well-dispersed mixed oxide species. For samples calcined at 900 °C, the Cu bonded in monoclinic zirconia-based phase is reducible at higher temperatures, ~320 °C and the reduction process is completely finished at around 510 °C (Fig. 4b). Very small peak at ~460 °C could be attributed to the reduction of Cu<sub>2</sub>O [17]. Although the presence of Cu<sub>2</sub>O was not evidenced by XRD nor by XPS, the presence of a very low percentage, below the limit of detection equipment, cannot be completely ruled out. Cu<sub>2</sub>O may be formed as a result of random distributions of the oxygen vacancy generated by the presence of Y<sup>3+</sup>, Cu<sup>2+</sup> and Ti<sup>4+</sup> substituting Zr<sup>4+</sup> ions. Detailed investigations of the reduction mechanism for Cu<sub>2</sub>O demonstrated that it is less reducible, having apparent activation energy 27.4 kcal/mol compared to CuO 14.5 kcal/mol [18]. On the other hand, embedding Cu<sub>2</sub>O into the matrix YSZ using our direct synthesis method, can make Cu<sub>2</sub>O less reducible with complete reduction at ~510 °C. The increases in the reduction temperature can be explained by the significant growth of crystalline sizes for both the zirconia-based main phase (from 8 to 30 nm), and CuO (from 12 to 25 nm) (Table 2) with the calcination temperature and in agreement with the literature data [19].

As revealed by XRD analysis, after thermal treatment, the Ni containing samples possess mainly fluorite-type phase and a secondary phase isostructural with bunsenite (NiO). Consequently, the reduction degree of the Ni is strongly affected by these structural properties. The TPR profile of NTST700 and NTST900 (Fig. 4c, d) consists of two main peaks corresponding to the reduction of the different Ni species: i) in the temperature range 350–400 °C, NiO from the surface and Ni from the subsurface is reduced to metallic Ni [20] ii) the peak at around 600 °C is assigned to the reduction of NiO species in intimate contact with the support [21]. Consistently with the XRD data, the TPR profile of the calcined NTST proves the absence of Ni<sub>2</sub>O<sub>3</sub>.

A shift to higher reduction temperature is observed for samples calcined at 900 °C, explained also in this case by the significant crystal growth of both phases, from 5 to 15 nm during the thermal treatment.

The XPS data were recorded for the CTST and NTST samples thermal treated at 700 °C and 900 °C, respectively (Figs. 5 and 6).

For data processing and interpretation, we followed a critical review of the available databases [22] and the literature.

**Table 2**  
Structural and textural properties of the anode materials after the thermal treatment at different temperatures.

Sample	Surface area (m <sup>2</sup> /g)	Average pore volume (cm <sup>3</sup> /g)	Average pore diameter (nm)	Crystallite size, d <sup>a</sup> (nm)
CTST700	15	0.077	13.4	8/12 <sup>b</sup>
CTST900	1	0.03	60	30/25 <sup>b</sup>
NTST700	66	0.173	7.4	5/5 <sup>b</sup>
NTST900	8	0.120	47	15/15 <sup>b</sup>

<sup>a</sup> Determined from XRD data.

<sup>b</sup> For secondary phase.

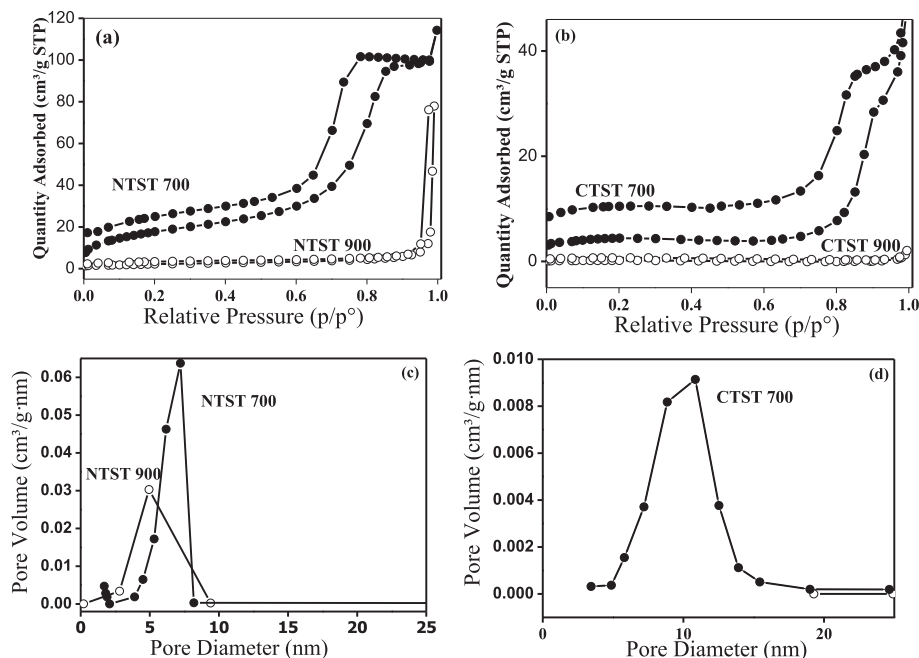


Fig. 2. N<sub>2</sub> adsorption/desorption isotherms (a–b) and pore size distribution (c–d) for the CTST and NTST samples thermal treated at 700 and 900 °C.

Additionally, standards CuO, NiO, TiO<sub>2</sub>, ZrO<sub>2</sub> and Y<sub>2</sub>O<sub>3</sub> samples were measured to ensure reliable assignments to the photoelectron lines, as well as to compare the Cu2p and Ni2p signature doublets shapes. After data processing, the XPS results are summarized in Figs. 5 and 6 and Table 3. While Cu2p and Ni2p transitions exhibit a complex structure, Ti2p, Zr3d and Y3d prominent

XPS transitions display typically 4+, 4+ and 3+ oxidation states, respectively.

A close inspection of Cu2p photoelectron spectra (Fig. 5a) reveals the presence of Cu<sup>2+</sup> oxidation state for CTST700 and CTST900 samples following the assignments of the binding energies, as well as the associated shake-up satellites and their

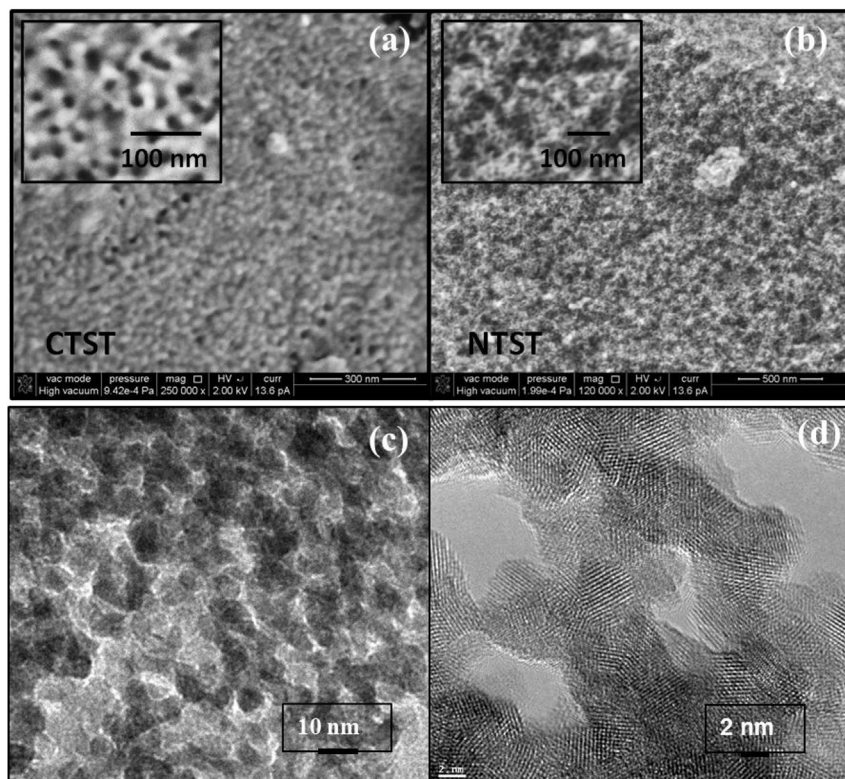


Fig. 3. SEM micrographs of the CTST (a), NTST (b) samples calcined at 700 °C and TEM micrographs (c,d) of NTST700.

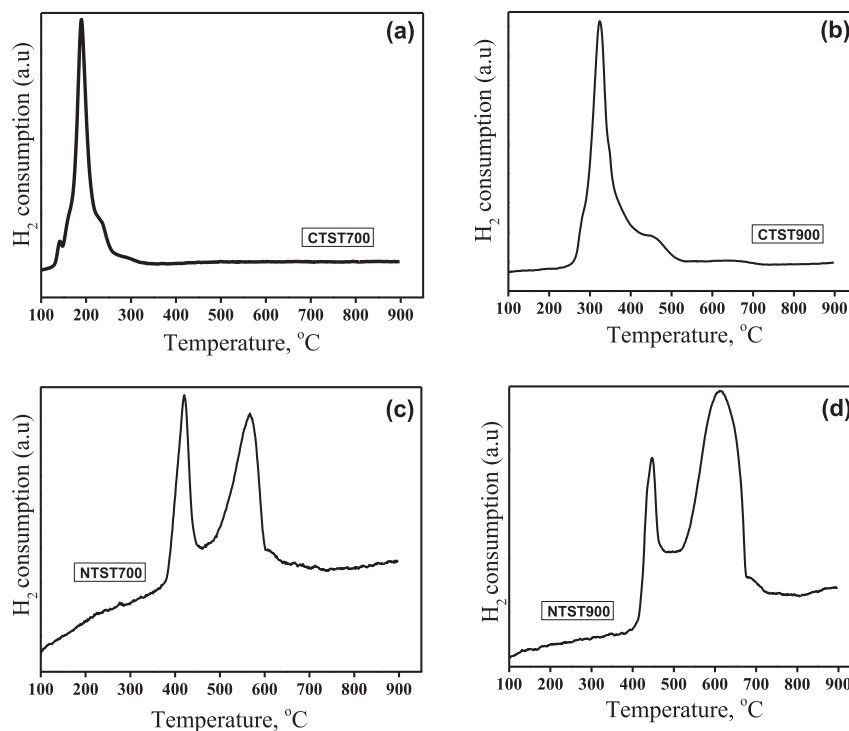


Fig. 4. TPR profile for CTST700 (a), CTST900 (b), NTST700 (c) and NTST900 (d) samples.

relative intensities, in agreement with XRD results.

Nevertheless, Ni2p doublet shows typical characteristics of the 2+ oxidation state (Fig. 5b) related to the binding energies, satellite structure and the overall spectral shape. The deconvolution of the O1s singlet highlights mainly oxygen bonded in the lattice as  $O^{2-}$  as well as the OH groups and  $H_2O$  adsorbed on the outermost surface layer (Fig. 6a inset). One can notice that the thermal treatment does not produce significant changes in the oxygen chemistry, the surface remaining hydroxylated even at high temperature.

The quantification was made from high resolution spectra with the sensitivity factors (SFs) checked from standard samples and following the protocol recommended by ISO-TC201 – “Quantitative analysis”. The data obtained are summarized in Table 3.

Regarding CTST sample, a segregation/diffusion phenomenon is clearly observed. Thus, with increasing temperature, the surface region is depleted in Ti and Cu and enriched in Y and Zr. A diffusion process of Ti and Cu from the surface to the bulk/subsurface takes place. This is clearly visible in Fig. 5a after a closer inspection of the superimposed spectra. A direct comparison can be established,

since the total number of scans over the binding energy ranges for Ti2p and Cu2p doublets were kept.

The spectra collected for the CTST900 sample display an increased level of noise as compared to the CTST700 sample suggesting lower relative concentrations for Cu and Ti. A cross correlation could be made after an inspection of Y3d (more pronounced) and Zr3d (less pronounced due to relative high concentrations) superimposed spectra (Fig. 6b–d).

### 3.2. Catalytic tests

Catalytic properties were evaluated through the partial oxidation of methane which has been performed for the two compositions. Firstly, blank tests were performed in the presence of quartz wool alone, by using the same reaction parameters as during the catalyst screening, showing no detectable occurrence of homogeneous reactions. To compare catalytic activity and selectivity of the various catalysts as a function of the detected products in the reaction stream, we assumed the following set of reactions to take

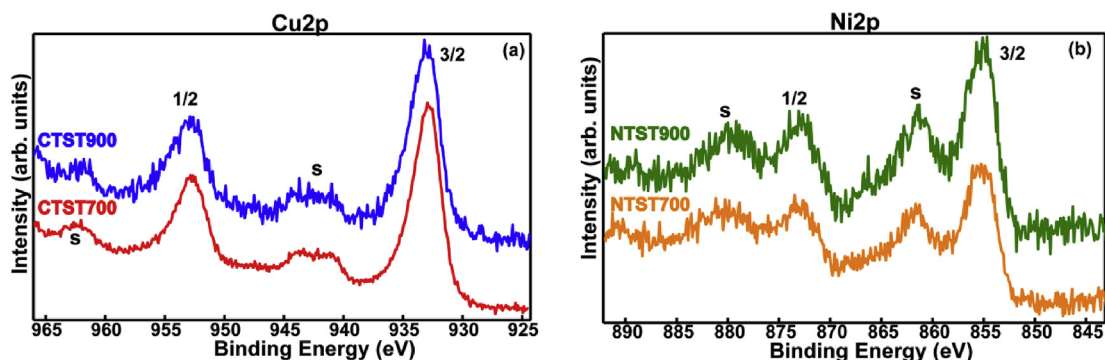


Fig. 5. The Cu2p and Ni2p photoelectron high resolution spectra for the CTST and NTST samples calcined at 700 °C and 900 °C, respectively.

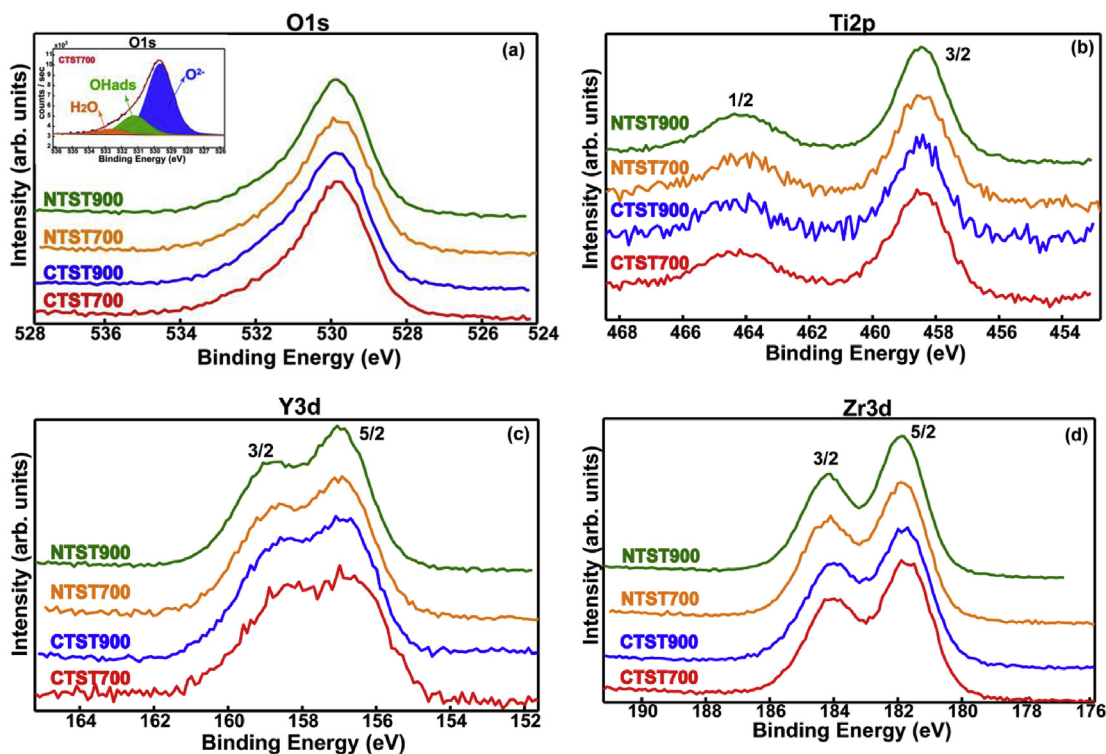


Fig. 6. The O1s, Ti2p, Y3d and Zr3d photoelectron high resolution spectra for the CTST and NTST samples calcined at 700 °C, 900 °C.

Table 3

Binding energies and surface cation relative concentration results from the XPS measurements in CTST and NTST samples after different treatments.

Sample	Binding energies, eV					Cation relative concentrations				
	Cu2p3/2	Ni2p3/2	Ti3/2	Y3d5/2	Zr5/2	Cu	Ni	Ti	Y	Zr
CTST700	933.3	–	458.2	157.2	181.8	36	–	14.9	7.4	41.7
CTST900	933.4	–	458.2	157.3	181.9	12.2	–	6.4	20.1	61.4
NTST700	–	854.8	458.2	157.2	181.9	–	12.8	12.5	16.8	57.9
NTST900	–	854.8	458.2	157.2	181.9	–	9.0	9.2	19.1	62.7

place on our catalysts: syngas production Eq (3) and total oxidation of CH<sub>4</sub>, producing CO<sub>2</sub> and H<sub>2</sub>O Eq (4):



Figs. 7 and 8 present the effect of calcination temperature on the catalytic activity and selectivity on each sample. The methane conversion values were taken after 30 min of reaction at each

temperature. Products of methane oxidative coupling (C<sub>2</sub> and higher hydrocarbons) were not observed on the entire temperature range studied.

The conversion profile recorded for the catalytic partial oxidation of methane (Fig. 7, a and b) showed that CTST materials are active above 400 °C, while NTST materials are active only above 600 °C with methane completely converted at 850 °C and a selectivity of almost 100% in CO. On the other hand, the O<sub>2</sub> consumption of CTST900 sample is observed at considerably lower temperature (200 °C) with respect to the NTST900 system (450 °C). This

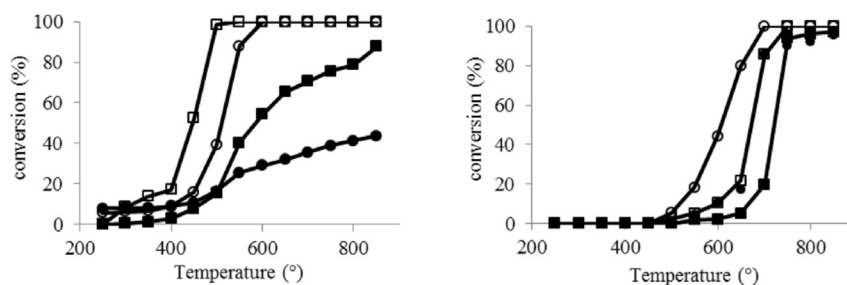


Fig. 7. Methane conversion (full symbols) and oxygen conversion (empty symbols) on (a) CTST and (b) NTST samples; circles – for the samples calcined at 700 °C and square for the samples calcined at 900 °C (CH<sub>4</sub>:O<sub>2</sub> = 2:1; total flow of 37.5 mL min<sup>-1</sup> and GHSV of 22500 h<sup>-1</sup>).

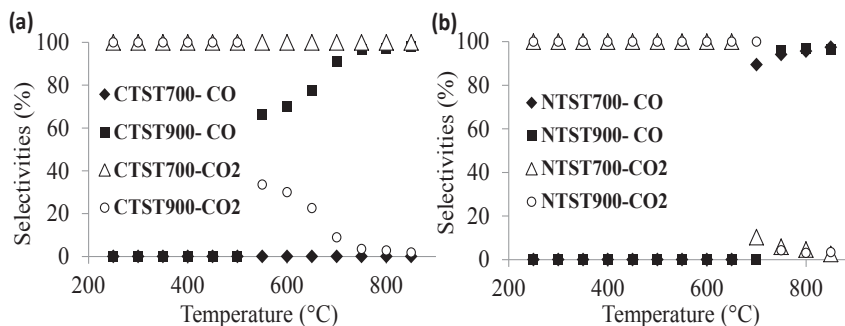


Fig. 8. CO and CO<sub>2</sub> selectivities on (a) CTST and (b) NTST samples.

consumption continues up to about 350 °C and can be related to the partial oxidation of Cu particles, due to the fact that no methane conversion was observed. The concomitant conversions of CH<sub>4</sub> and O<sub>2</sub> start above 400 °C. Up to 550 °C, only CO<sub>2</sub> and H<sub>2</sub>O are detected according with eq. (2) (Fig. 8a). At this temperature for CTST900, complete conversion is achieved for O<sub>2</sub> and, simultaneously, H<sub>2</sub> and CO sharply increases according with eq. (3).

However for NTST sample, this consumption of O<sub>2</sub> continues up to about 600 °C and can also be related to the partial oxidation of Ni particles, as previously reported [23]. For NTST system the associated conversions of CH<sub>4</sub> and O<sub>2</sub> start up at 600 °C, where only CO<sub>2</sub> and H<sub>2</sub>O are detected. Nevertheless, the complete conversion of O<sub>2</sub> takes place above 750 °C, whereas the H<sub>2</sub> and CO production increases drastically (Figs. 7 and 8 b).

As can be observed from Figs. 7 and 8, the catalytic behavior in POM of CTST system is very different from NTST samples. The samples containing Ni are more active than those containing Cu, with 90% conversion at 750 °C for NTST900 as compared to 75% methane conversion for CTST900, even though, for NTST system the CH<sub>4</sub> conversion starts at higher temperatures (600 °C vs 400 °C for CTST). The situation is different in the case of CTST samples, calcined at different temperatures; CTST900 is more active for methane selective oxidation than CTST700. XRD analysis has shown a phase transition of CTST when the sample is annealed at high temperature (900 °C). The monoclinic structure at 900 °C allows the production of CO [24], whereas CTST700, which presents cubic phase of fluorite type, is only selective in all the operation temperature range, to CO<sub>2</sub>. In the case of Ni containing samples, the calcination temperature does not affect the crystalline phase, and therefore the catalytic activity is not much affected neither.

As it has been previously reported [23,25], the CH<sub>4</sub> combustion takes place on NiO, while the reforming of CH<sub>4</sub> is promoted by Ni reduced in situ at high temperature. The CO formation at higher temperatures for NTST system can also be attributed to the NiO reduction into Ni<sup>0</sup> by CH<sub>4</sub>, which occurs at a certain critical temperature, besides the complete oxidation of methane. The fact that nickel valence changes during the reaction, represents an important parameter, which is responsible for the transformation of the reaction from complete oxidation to partial oxidation of methane (Fig. 7b). On NTST samples, in the first step of the reaction, the active centers are NiO species, which are formed by oxidation of metallic species at low temperature (until 550 °C), followed by a second step in which the metal oxide particles are reduced at higher temperature (750 °C) and represent the active centers responsible for the partial oxidation of methane. As already reported, the Ni<sup>0</sup> species constitute the active sites for the POM [21]. In addition, L. de Rogatis et al. [21] studied the influence of Cu and Ni in the CH<sub>4</sub> reforming reaction. Ni reduced in-situ showed better results and lower initial temperature reaction, evidencing a strong influence of the Ni particles size. This way, the difference obtained

in the activity between NTST700 and NTST900 can be attributed to the modification of particle size that was reported by XRD results. Furthermore, Cu based catalyst studied in their research, showed the lowest performance for the partial oxidation of CH<sub>4</sub>, in agreement with our results obtained for CTST samples.

Except for the CTST700 sample, on which no CO formation was recorded, the selectivity of CO increases with the reaction temperature, in detriment of CO<sub>2</sub> formation (Fig. 8), as thermodynamically expected. The full CH<sub>4</sub> oxidation according with eq. (4) giving rise to CO<sub>2</sub> and H<sub>2</sub>O observed on CTST700, could be related to reduction of CuO present in the initial oxidized catalyst, which becomes fully reduced during the CH<sub>4</sub> oxidation [26].

For the Cu containing sample CTST900, the formation of CO was recorded at 550 °C, whereas the CO production in Ni containing samples started at around 700 °C.

Previous observations in the literature [27,28], showed that the CH<sub>4</sub> transformation on pure CuO, basically, involves only generation of full oxidation products. The fact that only full oxidation product CO<sub>2</sub> is generated for CTST700 sample, suggests that mainly CuO is involved in the process. The presence of CuO was evidenced by XPS analysis. Also, the time needed for the CO formation for the CTST900 sample, indicates that during the process some reduction of CuO by CH<sub>4</sub> is firstly achieved, with the generation of active sites for the CO production.

Also, the catalytic stability is enhanced for the samples containing nickel (see the supplementary information). Due to smaller particle size, a higher cooking resistance and reaction stability of catalyst is expected [29,30]. Indeed, the particle size is responsible,

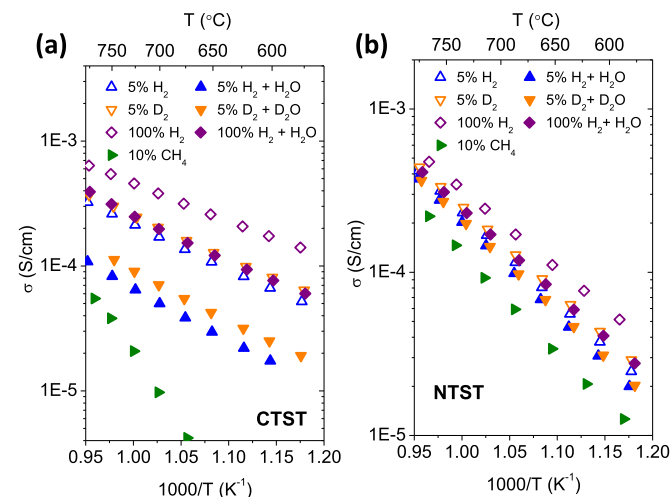


Fig. 9. Arrhenius plot of conductivity as function of different temperatures in reducing atmospheres.

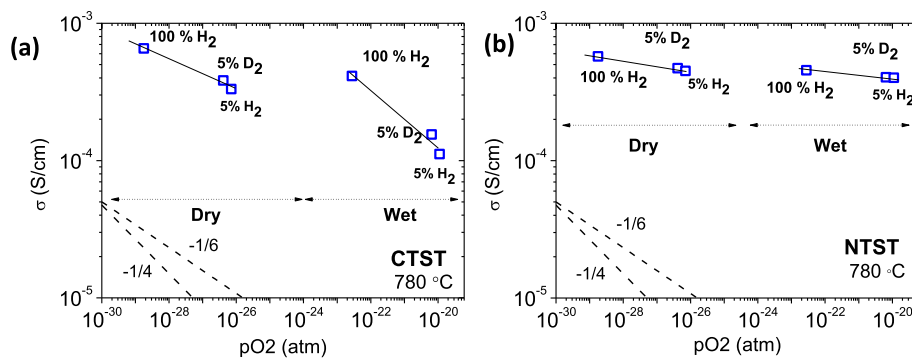


Fig. 10. Total conductivity as function of  $pO_2$  at 780 °C.

on one hand, for the catalytic stability, which is higher for NTST samples, as compared with CTST samples, for both calcination temperatures. On the other hand, it seems that the lower the particle size is, the higher the activity and selectivity are obtained [4]. NTST700 with the smallest crystallite size, obtained from XRD analysis, is active to CO, with 100%  $CH_4$  conversion at 700°C, whereas NTST900 needs 50°C more to produce CO and to reach 90% conversion.

### 3.3. DC conductivity measurements

In order to check the electronic properties of the materials synthesized, NTST and CTST were tested by means of DC conductivity measurements. Conductivity was analyzed as a function of temperature, oxygen partial pressure, water partial pressure and H/D isotopic effect to get insight into the nature of the conduction processes in the material. Specifically, CTST and NTS total conductivity measurements are presented in Figs. 9 and 10 as a function of the temperature in  $H_2$ ,  $D_2$ ,  $H_2$   $pH_2O$ ,  $D_2$   $pD_2O$  and 10% of  $CH_4$  in Ar

(where  $H_2$  and  $D_2$  (5%) are diluted in He and  $pH_2O$  and  $pD_2O$  are 0.025 atm) reducing atmospheres.

Figs. 9–11 shows constant conductivity activation energy ( $E_A$ ) in all conditions and for the different samples in the temperature range measured, with higher  $E_A$  for NTST. However, the behavior of the different samples in methane containing atmospheres changes drastically. The copper containing sample presents considerably lower total conductivity with a high  $E_A$ , whereas NTST maintains the  $E_A$  obtained in  $H_2$  and  $D_2$  atmospheres, but decreasing the total conductivity. This observation is directly related to the associated variations in  $pO_2$  and the nature of the conduction under these conditions.

As can be ascribed from Fig. 10, NTST shows a predominately ionic conductivity since the conductivity is almost  $pO_2$ -independent. However, CTST has a predominately n-type conductivity (with a  $pO_2$  dependence between  $-1/4$  and  $-1/6$ ) [31]. Furthermore, CTST exhibits a small ionic conductivity contribution since there is a slight deviation in the theoretical  $pO_2$  dependence ( $-1/4$ ,  $-1/6$ ). Additionally, in both cases the conductivity shows a non-

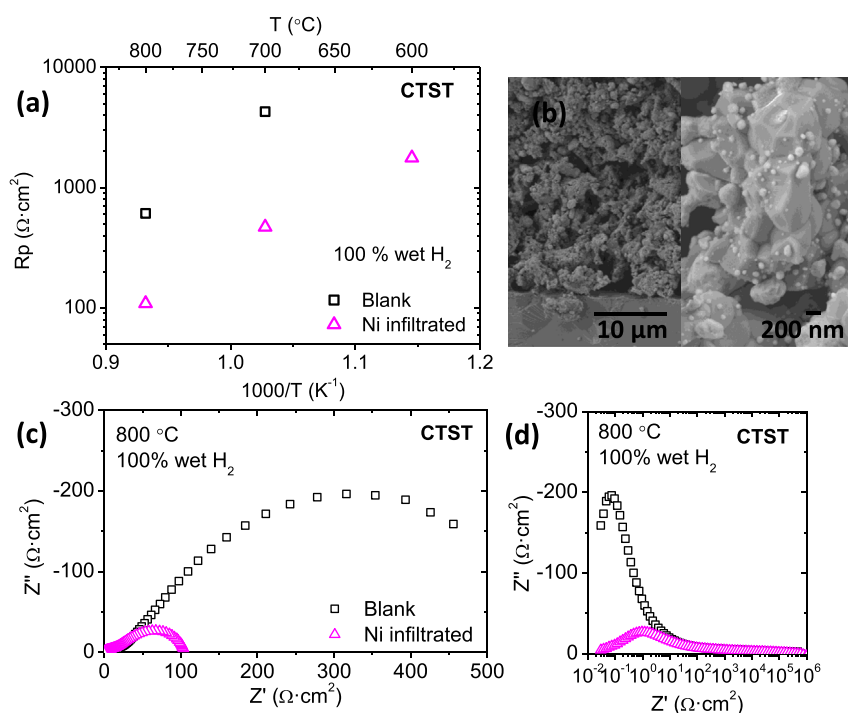


Fig. 11. (a) Polarization resistance as function of temperature, (b) FESEM micrographs of the electrode and electrolyte (left) and electrode magnification with Ni nanoparticles (right), (c) Nyquist and (d) Bode plot of EIS response of CTST infiltrated and not infiltrated.

proton transport, since there is neither hydration effect ( $\sigma_{\text{H}_2} > \sigma_{\text{H}_2 + \text{H}_2\text{O}}$  and  $\sigma_{\text{D}_2} > \sigma_{\text{D}_2 + \text{D}_2\text{O}}$ ) nor H/D isotopic effect ( $\sigma_{\text{D}_2 + \text{D}_2\text{O}} > \sigma_{\text{H}_2 + \text{H}_2\text{O}}$ ) in the temperature range measurements for both samples. NTST has maintained the conductivity behavior of the YSZ state of the art (ionic conductor) [32] whereas for Cu incorporated in the material the electronic conductivity prevails.

On the other hand, oxygen-deficient nonstoichiometry and oxygen conducting oxides play an important role in the catalysis process such as dehydrogenation reactions and partial oxidation of methane, due to the lattice oxygen  $\text{O}^{2-}$  [33]. CO and  $\text{H}_2$  can be obtained via the partial oxidation of methane, since methane can react with mobile lattice oxygen ( $\text{O}^{2-}$ ). The partial oxidation of methane produces oxygen vacancies ( $\text{Vo}^\cdot$ ) in the oxide that can be regenerated with oxygen or air. That fact can also support the best results obtained for NTST, since it has a predominately ionic conductivity and oxygen vacancies are key in the reaction mechanism.

### 3.4. EIS analysis of CTST compound

Symmetrical cell of CTST700 powders was prepared on dense YSZ electrolyte. Firstly, the blank electrode was tested by means of EIS measurements in 100% wet  $\text{H}_2$ . As can be ascribed from Fig. 11c and d there is a big contribution of the resistance at low frequency (LF) in the EIS spectra for the blank sample. This LF resistance is usually associated with surface processes, as dissociation, adsorption, etc. [34]. In order to reduce the LF resistance associated with the catalytic activity of the electrode, some improvement was performed. The blank sample was infiltrated with a Ni precursor solution after EIS measurements. New EIS measurements were carried out in the same operation temperatures and atmospheres, wet  $\text{H}_2$  (2.5% vol. of  $\text{H}_2\text{O}$ ). The LF resistance was reduced in the whole range of temperatures measured and the  $R_p$  decreased around five times from the initial electrode (Fig. 11 a).

From Fig. 11 b and c the huge reduction of the resistance at low frequencies can be highlighted, showing the important role of nanoparticles as catalyst [35] and the good performance of Ni for the hydrogen oxidation.

The anode porosity as well as electrolyte density can be observed in the cross-section image Fig. 11b. The cathode has enough porosity for the gas diffusion and relatively large surface area for the Ni deposition. Furthermore, in Fig. 11 b right it can be appreciated the Ni nanoparticles infiltrated. As can be shown in the SEM micrograph, the whole surface of the CTST was not covered with Ni nanoparticles, allowing the possibility of improving the cell's performance increasing the Ni content.

## 4. Conclusions

This study highlights a promising self-assembling synthesis route of (Ni/Cu, Ti)-YSZ (20 mol. % Ni/Cu, 10 mol.% Ti) templated by a nonionic surfactant – Triton X100. Various structural, catalytic and electrochemical characterizations were investigated, as well as the performance of these systems for hydrogen production through POM. In particular the main findings can be summarized as follows:

- The structural properties revealed that CTST exhibits a phase transition when the sample is calcined at 900 °C, changing from cubic fluorite phase to monoclinic, whereas NTST shows mainly cubic phase for both calcination temperatures. The secondary phases as CuO (Tenorite) and NiO (Bunsenite), respectively, were emphasized for CTST and NTST samples, while Ti was very well incorporated in the YSZ lattice.
- The assessment of the surface chemistry pointed out no changes in the oxidation states for different thermal treatments. Thus, Cu2p and Ni2p XPS transitions confirm only the presence of

2+ oxidation state, while Ti2p, Zr3d and Y3d prominent XPS transitions display typically 4+, 4+ and 3+ oxidation states for both calcination temperatures. Hydroxylated surfaces were found for the CTST and NTST samples calcined at both temperatures.

- The samples containing Ni are more active in POM than those containing Cu. CTST700 has no activity for the partial oxidation of methane, whereas the monoclinic phase CTST900 has obtained good results above 700 °C. Total combustion of  $\text{CH}_4$  occurs on the oxidized particles, while partial oxidation of  $\text{CH}_4$  takes place on reduced particle.
- The conductivity measurements performed in  $\text{H}_2$ ,  $\text{D}_2$ ,  $\text{H}_2$  p $\text{H}_2\text{O}$ ,  $\text{D}_2$  p $\text{D}_2\text{O}$  and 10% of  $\text{CH}_4$  in Ar reducing atmospheres showed that NTST presents prevailing ionic conductivity whereas CTST shows mainly an n-type conductivity. The ionic conductivity of CTST can help the partial oxidation of methane due to the oxygen vacancies generated on the surface of the material, which play a fundamental role in the  $\text{O}_2$  activation mechanism.

## Acknowledgements

This work was supported by a grant of Partnerships in priority S&T domains Programm (PNII), MEN–UEFISCDI, PCCA1, project number 26/2012, ENE2011-24761 and Severo Ochoa SEV-2012-0267 grants.

## References

- [1] B.C. Steele, A. Heinzel, *Materials for fuel-cell technologies*, *Nature* 414 (2001) 345–352.
- [2] S.M. Haile, *Fuel cell materials and components*, *Acta Mater.* 51 (2003) 5981–6000.
- [3] B.S. Prakash, S.S. Kumar, S. Aruna, *Properties and development of Ni/YSZ as an anode material in solid oxide fuel cell: a review*, *Renew. Sust. Energ Rev.* 36 (2014) 149–179.
- [4] P. Gélin, M. Primet, *Complete oxidation of methane at low temperature over noble metal based catalysts: a review*, *Appl. Catal. B Environ.* 39 (2002) 1–37.
- [5] Z. Shao, W. Zhou, Z. Zhu, *Advanced synthesis of materials for intermediate-temperature solid oxide fuel cells*, *Prog. Mater. Sci.* 57 (2012) 804–874.
- [6] S. Jung, C. Lu, H. He, K. Ahn, R.J. Gorte, J.M. Vohs, *Influence of composition and Cu impregnation method on the performance of Cu/CeO<sub>2</sub>/YSZ SOFC anodes*, *J. Power Sources* 154 (2006) 42–50.
- [7] S. Somacescu, V. Parvulescu, P. Osiceanu, J.M. Calderon-Moreno, B.-L. Su, *Structure and surface chemistry in crystalline mesoporous (CeO<sub>2</sub>– $\delta$ )-YSZ*, *J. Colloid Interf. Sci.* 363 (2011) 165–174.
- [8] S. Casino, F. Di Lupo, C. Francia, A. Tuel, S. Bodoardo, C. Gerbaldi, *Surfactant-assisted sol gel preparation of high-surface area mesoporous TiO<sub>2</sub> 2 nanocrystalline Li-ion battery anodes*, *J. Alloys Compd.* 594 (2014) 114–121.
- [9] X. Han, W.-J. Qin, J. Sun, J. Yang, K.-Y. Niu, H.-L. Wang, X.-W. Du, *Surfactant-assisted synthesis of ZnO–Au nanostructure with good dispersibility*, *J. Alloys Compd.* 477 (2009) 661–664.
- [10] W. Wang, S.P. Jiang, A.I.Y. Tok, L. Luo, *GDC-impregnated Ni anodes for direct utilization of methane in solid oxide fuel cells*, *J. Power Sources* 159 (2006) 68–72.
- [11] H. You, C. Zhao, B. Qu, G. Guan, A. Abudula, *Fabrication of Ni 0.5 Cu 0.5 O x coated YSZ anode by hard template method for solid oxide fuel cells*, *J. Alloys Compd.* 669 (2016) 46–54.
- [12] H.S. Hong, S. Lee, *Fabrication and characterization of 900° C-sintered Ni/Cu/YSZ cermet high temperature electrolysis cathode material prepared by high-energy ball-milling method*, *J. Alloys Compd.* 538 (2012) 201–204.
- [13] S. Lee, K.-H. Kang, J.-M. Kim, H.S. Hong, Y. Yun, S.-K. Woo, *Fabrication and characterization of Cu/YSZ cermet high-temperature electrolysis cathode material prepared by high-energy ball-milling method: I. 900° C-sintered*, *J. Alloys Compd.* 448 (2008) 363–367.
- [14] S. Somacescu, J.M.C. Moreno, P. Osiceanu, B.-L. Su, V. Parvulescu, *Single-phase solid solution (TiO<sub>2</sub>)<sub>x</sub>-(YSZ)<sub>1-x</sub> mesoporous nanoparticles with catalytic activity in the oxidation of methane*, *J. Phys. Chem. C* 114 (2010) 19365–19372.
- [15] S. Somacescu, M. Florea, P. Osiceanu, J.M. Calderon-Moreno, C. Ghica, J.M. Serra, *Ni-doped (CeO<sub>2</sub>– $\delta$ )-YSZ mesostructured with nanocrystalline framework: the effect of thermal treatment on structure, surface chemistry and catalytic properties in the partial oxidation of methane (CPOM)*, *J. Nanopart. Res.* 17 (2015) 1–16.
- [16] S. Jiang, *Resistance measurement in solid oxide fuel cells*, *J. Electrochem. Soc.* 148 (2001) A887–A897.
- [17] G. Fierro, M. Lojacono, M. Inversi, P. Porta, R. Lavecchia, F. Cioci, *A study of anomalous temperature-programmed reduction profiles of Cu 2 O, CuO, and CuO-ZnO catalysts*, *J. Catal.* 148 (1994) 709–721.

- [18] J.Y. Kim, J.A. Rodriguez, J.C. Hanson, A.I. Frenkel, P.L. Lee, Reduction of CuO and Cu<sub>2</sub>O with H<sub>2</sub>: H embedding and kinetic effects in the formation of suboxides, *J. Am. Chem. Soc.* 125 (2003) 10684–10692.
- [19] J. Marrero-Jerez, E. Chinarro, B. Moreno, J. Peña-Martínez, P. Núñez, CGO<sub>20</sub>–CuO composites synthesized by the combustion method and characterized by H<sub>2</sub>-TPR, *Ceram. Int.* 41 (2015) 10904–10909.
- [20] C.-W. Hu, J. Yao, H.-Q. Yang, Y. Chen, A.-M. Tian, On the inhomogeneity of low nickel loading methanation catalyst, *J. Catal.* 166 (1997) 1–7.
- [21] L. De Rogatis, T. Montini, A. Cognigni, L. Olivi, P. Fornasiero, Methane partial oxidation on NiCu-based catalysts, *Catal. Today* 145 (2009) 176–185.
- [22] C.D. Wagner, A.V. Naumkin, A. Kraut-Vass, J.W. Allison, C.J. Powell, J.R. Rumble Jr., NIST standard reference database 20, in: NIST XPS Database Version, vol. 3, 2003, pp. 251–252.
- [23] R. Jin, Y. Chen, W. Li, W. Cui, Y. Ji, C. Yu, Y. Jiang, Mechanism for catalytic partial oxidation of methane to syngas over a Ni/Al<sub>2</sub>O<sub>3</sub> catalyst, *Appl. Catal. A Gen.* 201 (2000) 71–80.
- [24] A.C. Ferreira, A. Ferraria, A.B. do Rego, A.P. Gonçalves, A.V. Girão, R. Correia, T.A. Gasche, J.B. Branco, Partial oxidation of methane over bimetallic copper–cerium oxide catalysts, *J. Mol. Catal. A Chem.* 320 (2010) 47–55.
- [25] Y. Lu, J. Xue, C. Yu, Y. Liu, S. Shen, Mechanistic investigations on the partial oxidation of methane to synthesis gas over a nickel-on-alumina catalyst, *Appl. Catal. A Gen.* 174 (1998) 121–128.
- [26] A. Hornés, P. Bera, M. Fernández-García, A. Guerrero-Ruiz, A. Martínez-Arias, Catalytic and redox properties of bimetallic Cu–Ni systems combined with CeO<sub>2</sub> or Gd-doped CeO<sub>2</sub> for methane oxidation and decomposition, *Appl. Catal. B Environ.* 111 (2012) 96–105.
- [27] L. Kundakovic, M. Flytzani-Stephanopoulos, Cu- and Ag-modified cerium oxide catalysts for methane oxidation, *J. Catal.* 179 (1998) 203–221.
- [28] C. Au, Y. Hu, H. Wan, Methane activation over unsupported and La<sub>2</sub>O<sub>3</sub>-supported copper and nickel catalysts, *Catal. Lett.* 36 (1996) 159–163.
- [29] S. Xu, R. Zhao, X. Wang, Highly coking resistant and stable Ni/Al<sub>2</sub>O<sub>3</sub> catalysts prepared by W/O microemulsion for partial oxidation of methane, *Fuel Process. Technol.* 86 (2004) 123–133.
- [30] J.B. Claridge, M.L. Green, S.C. Tsang, A.P. York, A.T. Ashcroft, P.D. Battle, A study of carbon deposition on catalysts during the partial oxidation of methane to synthesis gas, *Catal. Lett.* 22 (1993) 299–305.
- [31] W. Gao, N.M. Sammes, *An Introduction to Electronic and Ionic Materials*, World Scientific, 1999.
- [32] S.T. Revankar, P. Majumdar, *Fuel Cells: Principles, Design, and Analysis*, CRC Press, 2014.
- [33] M.S.S. Khine, L. Chen, S. Zhang, J. Lin, S.P. Jiang, Syngas production by catalytic partial oxidation of methane over (La<sub>0.7</sub>A<sub>0.3</sub>)BO<sub>3</sub> (A= Ba, Ca, Mg, Sr, and B= Cr or Fe) perovskite oxides for portable fuel cell applications, *Int. J. Hydrogen Energy* 38 (2013) 13300–13308.
- [34] S.B. Adler, Factors governing oxygen reduction in solid oxide fuel cell cathodes, *Chem. Rev.* 104 (2004) 4791–4844.
- [35] L. Navarrete, C. Solís, J. Serra, Boosting the oxygen reduction reaction mechanisms in IT-SOFC cathodes by catalytic functionalization, *J. Mater. Chem. A* 3 (2015) 16440–16444.